Transactions on Computer Science and Intelligent Systems Research
ISSN: 2960-1800, eISSN: 2960-2238 | Volume 12
ESAC 2026

# Physical Model Construction and Robust Parameter Inversion for Infrared Interferometric Spectroscopy Measurement of Silicon Carbide Epitaxial Layer Thickness

Sibo Wang [1, *], Shiqi Li [2], Hao Huang [2]

[1] College of Aviation Engineering, Civil Aviation Flight University of China, Chengdu, China, 618307

[2] Faculty of Science, Civil Aviation Flight University of China, Chengdu, China, 618307

* Corresponding Author Email: yiusd13212596@163.com

**Abstract.** This paper establishes a physical model and designs a robust inversion algorithm for the precise measurement of silicon carbide epitaxial layer thickness. First, under the dual-beam interference assumption, a physical dual-beam interference model for silicon carbide epitaxial layer thickness was developed. This model, based on optical path difference and phase analysis, dynamically calculates refractive index using the Sellmeier dispersion model. It quantifies beam amplitude differences through Fresnel reflection coefficients, constructing a complete total internal reflection model that satisfies energy conservation. Subsequently, a dispersion-coupled nonlinear inversion and reliability assessment scheme for epitaxial layer thickness was designed for measured spectral data. This scheme employs data preprocessing to construct a nonlinear least-squares model targeting minimization of residuals between measured and modeled reflectance. The TRF algorithm and robust loss function are then jointly optimized to determine thickness and Sellmeier parameters. Ultimately, the optimal thickness estimate was obtained. The reliability of the results was comprehensively evaluated using Bootstrap resampling, error analysis, and multi-angle consistency verification. This research provides a highly accurate and reliable measurement framework, which is crucial for quality control and process optimization in the manufacturing of high-performance silicon carbide semiconductor devices.

**Keywords:** Infrared Interferometry; Sellmeier Dispersion Model; Nonlinear Least-Squares Optimization.

## 1. Introduction

Infrared interferometry, as a non-destructive and high-precision measurement technique, serves as a crucial method for determining the thickness of silicon carbide (SiC) epitaxial layers, which is a key parameter for the performance and yield of SiC-based power electronic devices. When infrared light is incident on the epitaxial layer structure [1, 2], the two beams reflected from the air-epitaxial layer interface and the epitaxial layer-substrate interface produce characteristic interference fringes. The thickness of the epitaxial layer is jointly determined by parameters such as the infrared wavelength, the epitaxial layer refractive index, and the angle of incidence. However, the refractive index of semiconductor epitaxial layers is not constant; its variation with wavelength, known as the dispersion effect, is an inherent material property. Neglecting this dispersion leads to significant inaccuracies in the calculated optical path difference and introduces systematic errors in thickness determination [3, 4].

A review of existing literature reveals several common approaches for extracting film thickness from interference spectra. The traditional extrema method [5, 6], which calculates thickness based on the spacing between adjacent interference peaks or valleys, is straightforward but often assumes a constant refractive index, making it susceptible to errors from dispersion. Fourier transform-based methods [7, 8] can improve robustness to some extent by transforming the spectrum into the path difference domain. However, their accuracy can be compromised by the limited spectral range and windowing effects. Furthermore, many existing models operate under the assumption of

perpendicular incidence or neglect the amplitude differences between the two interfering beams described by Fresnel coefficients, which becomes increasingly invalid for non-perpendicular incidence scenarios essential for enhancing measurement sensitivity [9, 10]. While some advanced studies have incorporated dispersion models, the joint inversion of thickness and dispersion parameters often faces challenges of non-convexity and sensitivity to initial values and spectral noise, lacking a comprehensive framework for reliability assessment.

Therefore, to address these identified gaps, this study aims to resolve two core challenges: First, establishing a dual-beam interference physical model for silicon carbide epitaxial layer thickness that fully accounts for dispersion effects and amplitude differences under non-perpendicular incidence; Second, designing a dispersion-coupled nonlinear inversion and reliability assessment algorithm for epitaxial layer thickness based on this precise model, enabling robust extraction of thickness parameters from measured reflectance spectra and quantitative reliability analysis.

The marginal contributions of this paper are threefold:

A Comprehensive Physical Model: We develop a total reflection model that integrates the Sellmeier dispersion equation for dynamic refractive index calculation and Fresnel coefficients for amplitude quantification, ensuring energy conservation and moving beyond the limitations of constant-refractive-index and perpendicular-incidence assumptions.

A Robust Inversion Algorithm: We design a nonlinear least-squares optimization framework that jointly inverts the thickness and Sellmeier parameters. This framework leverages the Trust Region Reflective (TRF) algorithm combined with a robust loss function to effectively mitigate the influence of noise and outliers in the measured data.

A Rigorous Reliability Assessment: We implement a comprehensive evaluation scheme, including Bootstrap resampling for statistical uncertainty quantification and a multi-angle consistency test, to provide a credible confidence interval for the estimated thickness and validate the model's consistency.

To achieve this, the paper employs a three-step closed-loop approach (phase-extremum-wave number pitch) to derive the thickness-wave number relationship. Building upon this foundation, the nonlinear least-squares optimization is adopted for joint parameter inversion. The reliability of the results is comprehensively evaluated through statistical methods and multi-angle consistency tests, demonstrating the efficacy and robustness of the proposed methodology.

## 2. Physical Modeling of Silicon Carbide Epitaxial Layer Thickness via Dual-Beam Interferometry

### 2.1. Physical Background and Principle of Two-Beam Interference

The physical basis for measuring the thickness of silicon carbide epitaxial layers using infrared interferometry is the phenomenon of two-beam interference. When infrared light is incident on the epitaxial layer surface at a certain angle, two coherent beams are generated: one is directly reflected from the upper surface of the epitaxial layer (Reflected Beam 1), and the other penetrates the epitaxial layer, is reflected at the substrate interface, and then transmits out (Reflected Beam 2). These two beams produce an optical path difference due to different propagation paths, and when they meet, interference occurs, forming periodic interference fringes. The thickness of the epitaxial layer can be inverted by analyzing the spacing characteristics of the interference fringes.

### 2.2. Theoretical Derivation of Thickness Calculation Formula

#### 2.2.1. Analysis of Phase Difference and Optical Path Difference

Let the wavelength of infrared light be $\lambda$, the refractive index of the epitaxial layer be $n$, the thickness of the epitaxial layer be $d$, the incident angle of infrared light in air be $\theta_0$, and the refraction angle be $\theta_1$. When infrared light enters the epitaxial layer from air, it must follow the law of refraction,

which describes the quantitative relationship between the incident angle and the refraction angle. The incident angle and refraction angle satisfy:

$$\sin\theta_1 = \frac{\sin\theta_0}{n} \tag{1}$$

The optical path difference between the two reflected beams is the core cause of the interference phenomenon, and the additional propagation path of Reflected Beam 2 needs to be analyzed emphatically [7]. Through geometric path analysis, the infrared light propagates along the refraction angle $\theta_1$ in the epitaxial layer, and the propagation in the epitaxial layer can be divided into two stages: "incident downward to the substrate" and "return upward to the air". The total length of the round-trip path is:

$$\frac{2d}{\cos\theta_1} \tag{2}$$

Furthermore, according to the conversion formula between optical path and geometric path, the additional optical path of Reflected Beam 2 is obtained as:

$$\Delta L = \frac{2nd}{\cos\theta_1} \tag{3}$$

Considering that the essence of the interference phenomenon is the phase difference rather than the optical path difference, it is necessary to convert the optical path difference into a phase difference. It is known that the phase change corresponding to the unit optical path is:

$$\frac{2\pi}{\lambda} \tag{4}$$

Therefore, the phase difference between the two reflected beams is:

$$\Delta\Phi = \frac{4\pi nd\cos\theta_1}{\lambda} \tag{5}$$

This formula is the core formula connecting physical parameters and interference phenomena, and subsequent interference conditions are derived based on this.

### 2.2.2. Establishment of Thickness Equation Based on Interference Extremum Conditions

The alternating light and dark fringes correspond to specific values of the phase difference: when the phase difference is an integer multiple of $2\pi$, the two beams reinforce each other, forming interference maxima; when the phase difference is an odd multiple of $\pi$, the two beams weaken each other, forming interference minima. This is the physical basis for establishing the thickness model [8].

Taking interference maxima as the analysis object, let k represent the interference order. The condition for the occurrence of interference maxima is:

$$\Delta\Phi = 2k\pi, k = 1,2,3\ldots \tag{6}$$

Substituting Equation (3) into Equation (4), we get:

$$2nd\cos\theta_1 = k\lambda \tag{7}$$

This formula directly establishes the correlation between the epitaxial layer thickness $d$ and the wavelength $\lambda$, refractive index $n$, and interference order $k$. However, since $k$ cannot be directly measured, further transformation is required to adapt to the experimental data.

### 2.2.3. Simplification of Thickness Formula Based on Wavenumber Spacing

Since the data provided in the attachments are wavenumbers and the interference order $k$ cannot be directly observed, it is necessary to eliminate $k$ through the wavenumber spacing of adjacent fringes to obtain a formula that can directly calculate $d$. The wavenumber is defined as the number of waves per unit length. Considering unit consistency, the conversion formula between wavenumber and wavelength is:

$$\lambda(\mu m) = \frac{10^4}{V(cm^{-1})} \tag{8}$$

Substituting it into Equation (5), we obtain:

$$2ndcos\theta_1 = k \times \frac{10^4}{V_k} \tag{9}$$

Using adjacent fringes to eliminate the interference order $k$, take two adjacent interference maxima, the $k$-th order and the $(k+1)$-th order, with corresponding wavenumbers $V_k$ and $V_{k+1}$ respectively.we get:

$$\begin{cases} 2ndcos\theta_1 = k \times \frac{10^4}{V_k} \\ 2ndcos\theta_1 = (k+1) \times \frac{10^4}{V_{k+1}} \end{cases} \tag{10}$$

After simplification and rearrangement, define the wavenumber spacing of adjacent interference maxima as $\Delta V = |V_{k+1} - V_k|$. Substituting it into the above equation, we obtain:

$$k = \frac{V_k}{\Delta V} \tag{11}$$

Finally, substituting Equation (7) into Equation (6) and simplifying, the thickness calculation formula is derived:

$$d = \frac{10^4}{2ncos\theta_1 \Delta V} \tag{12}$$

## 2.3. Comprehensive Reflection Model Integrating Dispersion and Amplitude Effects

### 2.3.1. Dispersion Effect

As indicated in the problem, the refractive index of the epitaxial layer varies with wavelength. Assuming a constant refractive index will directly lead to inaccurate phase difference calculations, and thus deviations in thickness calculations. Therefore, it is necessary to introduce the Sellmeier dispersion model to solve this problem [9, 10]. The Sellmeier dispersion model [3] is a classic formula describing the relationship between the refractive index and wavelength of transparent media. Its core is to quantitatively describe the dispersion law through a small number of physical parameters, providing a physically meaningful method for calculating the refractive index for the model. Let $\lambda$

represent the wavelength; this study introduces three constants $A$, $B$, and $C$ to quantitatively express $n_1$:

$$n_1^2(\lambda) = A + \frac{B\lambda^2}{\lambda^2 - C} \tag{13}$$

The introduction of the dispersion model avoids the limitations of the constant refractive index assumption, makes the phase difference calculation more accurate, and thus improves the thickness estimation accuracy. Meanwhile, the Sellmeier coefficients have clear physical meanings, which can enhance the physical authenticity of the model.

### 2.3.2. Fresnel Reflection Coefficients

The core of two-beam interference is the amplitude superposition of two coherent beams. To quantitatively describe the amplitude difference between the two beams, Fresnel reflection coefficients [4] are introduced. Let $r_s$ and $r_p$ represent the s-polarization and p-polarization reflection coefficients, respectively. Their formulas are as follows:

$$r_s = \frac{n_i\cos\theta_i - n_j\cos\theta_j}{n_i\cos\theta_i + n_j\cos\theta_j}, r_p = \frac{n_j\cos\theta_i - n_i\cos\theta_j}{n_j\cos\theta_i + n_i\cos\theta_j} \tag{14}$$

When light is incident from air to the epitaxial layer interface, $n_i = n_0$, $\theta_i = \theta_0$, $n_j = n_1$, $\theta_j = \theta_1$, and $r_{01}$ is obtained. When light is incident from the epitaxial layer to the substrate interface, $n_i = n_1$, $\theta_i = \theta_1$, $n_j = n_2$, and $r_{12}$ is obtained. The reflection coefficient of unpolarized light takes the arithmetic average of the two:

$$r = \frac{r_s + r_p}{2} \tag{15}$$

### 2.3.3. Transmission Coefficients

In the two-beam interference model, the reflection and refraction of light must satisfy the law of conservation of energy, that is, the sum of the reflected energy and transmitted energy at the interface of transparent media must be equal to the incident energy. Ignoring the transmission coefficients will directly lead to the incorrect estimation of the amplitude of Reflected Beam 2. Therefore, it is necessary to introduce transmission coefficients $t_0$ and $t_1$ to quantitatively describe the energy loss of Reflected Beam 2 when penetrating the medium interface:

$$t_0 = t_1 = \sqrt{1 - r^2} \tag{16}$$

### 2.3.4. Total Reflection Model

After listing the above reflection coefficients, transmission coefficients, and phase difference calculation formulas, let $R_{mol}(\lambda)$ represent the calculated value of the model reflection rate, and the total reflection model is obtained as:

$$R_{mol}(\lambda) = \left|\frac{r_0 + r_1 e^{i\Phi}}{1 + r_0 r_1 e^{i\Phi}}\right|^2 \tag{17}$$

## 3. Dispersion-Coupled Nonlinear Inversion and Reliability Assessment of Epitaxial Layer Thickness

### 3.1. Data Preprocessing

#### 3.1.1. Data Processing

Analyzing the graph, it is observed that the graph has strong volatility and obvious discrete points, and these two parts are processed as figure 1:

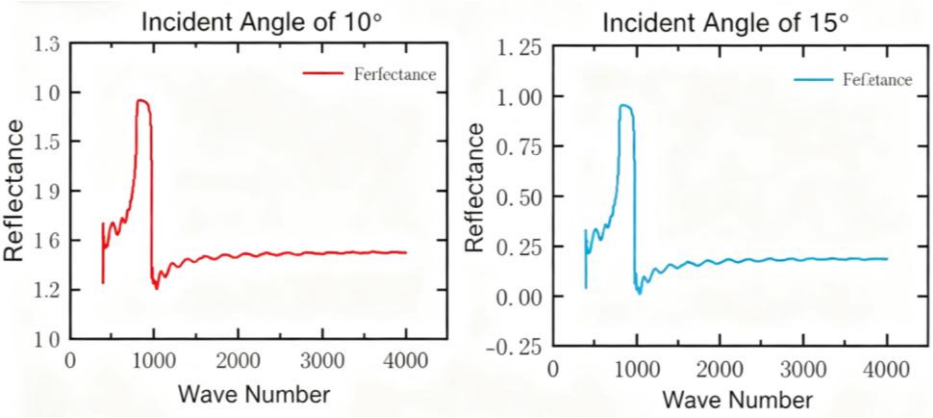


**Figure 1.** Relationship Between Incident Angle and Wavenumber Before Processing

To avoid physically unreasonable values, the reflectance is clipped to [0, 0.99]. The adaptive Savitzky-Golay method is used to slightly smooth the original reflection spectrum data to reduce the impact of noise.

#### 3.1.2. Decision on Handling Zero Values

It can be noted that the reflectance corresponding to the first wavenumber in both graphs is 0. From the data perspective, at this specific wavenumber of 399.6747 $cm^{-1}$, the corresponding light may exactly meet the condition of thin-film interference cancellation due to factors such as the thickness and refractive index of a certain optical thin-film structure, resulting in a reflectance of 0. It is also possible that under the current experimental environment, the incident angle of light at this wavenumber is exactly the Brewster angle [5].

Combined with the principle of infrared interferometry, this zero value conforms to the physical law of interference cancellation. Moreover, the zero value is a characteristic point of interference cancellation, and its corresponding wavenumber is a key known condition for solving the thickness. Considering that removing it will lose one interference extremum point, which may lead to an increase in subsequent thickness calculation errors, the zero value is retained.

### 3.2. Thickness Inversion Optimization Model

#### 3.2.1. Objective Function and Parameter Initialization

(1) Establishment of Objective Function

An optimization model is established, and nonlinear least squares fitting is used to jointly estimate the thickness $d$ and the refractive index parameters $A$, $B$, and $C$. Let $R_{mol}$ represent the calculated value of the model reflection rate, and $R_{obs}$ represent the reflection data at incident angles of 10° and 15°. The objective function is defined as minimizing the residual:

$$L(d, A, B, C) = \sum_{i\in\{10°,15°\}} \sum_{j=1}^{N_i} \left[R_{mol}(\lambda_{ij}; d, A, B, C, \theta_i) - R_{obs}(\lambda_i)\right]^2 \quad (18)$$

Where $R_{mol}$ is the theoretical predicted value based on physical theorems, and $R_{obs}$ is the measured experimental observation value.

(2) Initial Thickness Estimation

First, the initial thickness estimation is calculated according to the spacing of extremum points to provide a reasonable initial value for subsequent model fitting:

$$d = \frac{10^4}{2n_2 \cos\theta_1 \Delta V} \tag{19}$$

The data at incident angles of 10° and 15° are calculated respectively. When the incident angle is 10°, the initial thickness $d_{10} = 11.6414\ \mu m$ is calculated; when the incident angle is 15°, the initial thickness $d_{15} = 12.0578\ \mu m$ is calculated. Finally, the weighted average initial thickness $d = 11.8603\ \mu m$ is obtained. This initial value provides a reasonable starting point for subsequent parameter optimization, which helps to improve the convergence speed and accuracy of the optimization algorithm.

### 3.2.2. Solution Algorithm and Implementation

The TRF algorithm combined with a robust loss function is selected for parameter optimization. The TRF algorithm has good convergence when dealing with constrained least squares problems, and the robust loss function can effectively reduce the interference of noise peaks on the fitting process, making the model focus more on the overall trend of the data.

The goal of optimization is to minimize the residual between the model reflection rate and the experimental reflection rate. The parameters to be optimized include the epitaxial layer thickness $d$ and the parameters $A$, $B$, and $C$ in the Sellmeier refractive index dispersion model.

### 3.2.3. Thickness Inversion Results

Finally, based on the two-beam interference model and the Sellmeier dispersion model, the refractive index dispersion parameters are obtained as $A = 3.3593$, $B = 2.2827$, and $C = 0.099254$. The optimal thickness estimation of the silicon carbide epitaxial layer is: $d = 11.2496\mu m$. The multi-angle thickness estimation has good consistency, but the wide confidence interval is an area for improvement in accuracy.

## 3.3. Reliability Analysis of Calculation Results

To verify the reliability of the results, the model is subjected to reliability analysis.

### 3.3.1. Statistical Uncertainty Analysis Based on Bootstrap

To quantify the estimation uncertainty of model parameters (especially the epitaxial layer thickness d), this study adopts the Bootstrap resampling method for statistical inference. The Bootstrap sample trend graph [6] is a resampling method in statistics, whose core logic is "inferring the sample from the sample". The core process is as follows:

Resampling: Randomly draw data of the same size as the original sample with replacement from the original spectrum data to form a Bootstrap sample. Repeat this process $M = 1000$ times to generate 1000 Bootstrap sample sets.

Parameter Inversion: Substitute each Bootstrap sample set into the nonlinear least squares optimization model established in this study (Formula (12)) for refitting to obtain 1000 thickness estimation values $d$.

Distribution Construction and Uncertainty Quantification: According to the distribution of these 1000 $d^*$ values, calculate their 95% confidence interval and standard error to evaluate the statistical uncertainty of the thickness estimation value.

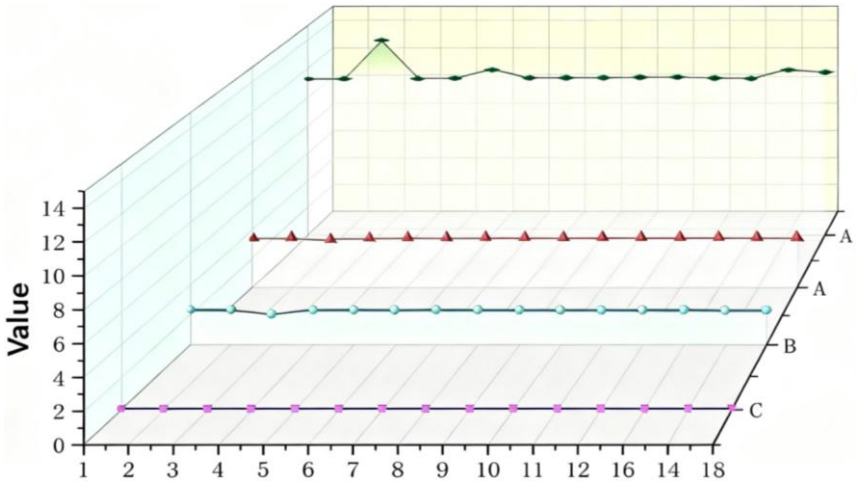


**Figure 2.** Bootstrap Sample Trend Graph

Bootstrap Sample Trend Graph is shown in figure 2. Different series (purple line, cyan line, red triangle, etc.) show stable numerical trends (e.g., the purple line is stably around 2, the cyan line is around 7–8, and the red line is around 12), with only one obvious peak in the green line above; the Bootstrap estimation variance of each statistic is small and stable, which not only reflects the robustness of the statistic to sample fluctuations but also verifies that the original statistic estimation has high accuracy, and the Bootstrap resampling can effectively capture the distribution characteristics of the statistic, but there is still room for improvement.

The data at 10° and 15° are visually analyzed using three parameters: RMSE, maximum error, and MAE.

For the data at 15° and 10°, the maximum error is significantly higher than the Root Mean Square Error (RMSE) and Mean Absolute Error (MAE). This indicates that there are individual points with large deviations in the data, and these outliers have a dominant impact on the "maximum error" indicator. In contrast, RMSE and MAE focus more on reflecting the average level of the overall error and are relatively less affected by extreme values. For RMSE, the RMSE of the data at 15° and 10° is about 0.3, which are relatively close. This indicates that from the perspective of "the mean of the squared errors and then taking the square root", the overall deviation degree between the model prediction and the actual data under the two incident angles is relatively close.

For MAE, the MAE of the data at 15° is about 0.25, and the MAE of the data at 10° is about 0.23, which are also relatively close. This reflects that the "average of the absolute deviations between the predicted values and the actual values" is at a similar level under the two incident angles, further confirming the consistency of the overall fitting effect of the model under different incident angles.

For the maximum error, the maximum error of both the data at 15° and 10° is close to 0.95. This indicates that there are a few abnormal cases where the error reaches a high level in both the 15° and 10° incident angle scenarios. However, since RMSE and MAE are relatively stable, these outliers do not have a decisive impact on the overall error evaluation.

### 3.3.2. Period Consistency Test

The core logic of the period consistency test is to compare the difference between the theoretical period and the measured period to evaluate the accuracy of fringe extraction and whether the model has systematic deviations. A table of period consistency verification results is drawn according to the output. Period Consistency Verification Results is shwon in table 1.

**Table 1.** Period Consistency Verification Results

| Incident Angle | Theoretical Period ($cm^{-1}$) | Measured Period ($cm^{-1}$) | Period Ratio |
|---|---|---|---|
| 10° | 187.44 | 170.18 | 1.10 |
| 15° | 188.06 | 163.87 | 1.15 |

The theoretical period and actual period of the fringes under the 10° incident angle scenario and the 15° incident angle scenario are compared. Finally, it is concluded that under the 10° incident angle scenario, the measured period is about 91% of the theoretical period, and under the 15° incident angle scenario, the measured period is about 87% of the theoretical period.

It can be seen that there is a certain degree of deviation, but the changing trends of the theoretical period and the measured period are consistent.

## 4. Conclusion

This study has successfully established a dual-beam interference physical model for silicon carbide (SiC) epitaxial layer thickness that comprehensively considers dispersion effects and amplitude differences. Based on this, a dispersion-coupled nonlinear inversion and reliability assessment scheme was designed. The proposed method effectively overcomes the systematic errors inherent in traditional approaches caused by neglecting refractive index variations and amplitude differences. Through robust nonlinear least-squares optimization, the joint inversion of thickness and Sellmeier dispersion parameters was achieved, yielding optimal thickness estimates for the SiC epitaxial layer. Results from Bootstrap resampling and multi-angle consistency tests demonstrate that the model and algorithm exhibit excellent stability and goodness-of-fit, fully validating their effectiveness for the precise determination of epitaxial layer thickness.

However, this study still has some limitations. For instance, the relatively wide confidence intervals of the inversion results indicate room for improvement in estimation accuracy. The fitting deviations at specific wavenumbers suggest that there may be physical factors not fully considered (such as surface roughness or interface transition layers). Furthermore, the current model primarily targets a single SiC homoepitaxial layer structure, and its broader applicability requires verification.

To address the above limitations, future research will focus on the following aspects:

Algorithm Optimization and Uncertainty Quantification: To address the issue of wide confidence intervals, we will explore more advanced optimization algorithms (such as combining the Levenberg-Marquardt algorithm with global optimization algorithms) and a Bayesian inversion framework. The Bayesian method can naturally provide the posterior probability distribution of parameters, enabling a more comprehensive quantification of the uncertainty in thickness and dispersion parameters, and yielding more reliable confidence intervals.

## References


[1] Zhang X, Chen R, Song F, et al. Machine-learning assisted glucose measurement system based on infrared photoacoustic spectroscopy [J]. Optics and Lasers in Engineering, 2025, 195109365-109365.

[2] Dante M, Vasiliki F, Javier G A, et al. Near-infrared photometry of the central stars of planetary nebulae with the VVVX survey [J]. Astronomy & Astrophysics, 2025, 702A79-A79.

[3] Ennass K, Remy B, Schick V, et al. Multi-spectral infrared thermography using finite element emissivity modelling for high-temperature measurements on metallic surfaces [J]. Infrared Physics and Technology, 2025, 150105999-105999.

[4] Rosales L A, Andrade M J, Tejedor G P, et al. Reliable methodologies to determine microplastics in mussels: Enhanced digestion protocols, transference to gold-coated filters and determination via laser-based transflectance infrared spectrometry [J]. Marine pollution bulletin, 2025, 222 (Pt 2): 118711.

[5] Kaplan I R, Girnis J, Sebastian A, et al. Patterns of prefrontal cortical activity associated with attention-demanding and motor aspects of dual-task walking as measured with functional near-infrared spectroscopy [J]. Behavioral neuroscience, 2025.10.19.

[6] Muthumanickam M, Palanivel R. GC-MS screening, characterization and in vitro antioxidant, antimicrobial and cytotoxic potential of gossypetin from Moringa oleifera [J]. Pharmacological Research - Natural Products, 2025, 8100332-100332.

[7] Zhou H, Li F, Sun N, et al. Non-Destructive Measurement of Sugar Content in Litchis Using Visible and Near-Infrared Spectroscopy and Fuzzy Stochastic Configuration Network [J]. Journal of food science, 2025, 90 (9): e70565.

[8] Hibner A, Tong K M, Liu L, et al. Multimodal Approach to Intraventricular Hemorrhage Using Echocardiography, Near-Infrared Spectroscopy, and Electrical Cardiometry in Preterm Infants [J]. Research square, 2025.10.19

[9] Addo D S K, Tengey K T, Boakye A, et al. Correction: Physico-mechanical measurements, functional properties, proximate composition of newly developed climate-resilient cowpea (Vigna unguiculata) varieties and their classification with near-infrared spectroscopy [J]. Food, Nutrition and Health, 2025, 2 (1): 25-25.

[10] Korsa A H, Bekele A E. Hydrothermally Synthesized CuV2O6/g-C3N4 Nanocomposite for Efficient Co (II) Removal: RSM Optimization, Adsorption Mechanism, and Reusability Study [J]. ACS omega, 2025, 10 (30): 33558-33569.